



# Microstructure, Mechanical and Corrosion Properties of AlCoCrFeNi High-Entropy Alloy Prepared by Spark Plasma Sintering

P. F. Zhou<sup>1</sup> · D. H. Xiao<sup>1</sup> · T. C. Yuan<sup>1</sup>

Received: 7 May 2019 / Revised: 30 July 2019 / Published online: 2 November 2019  
© The Chinese Society for Metals (CSM) and Springer-Verlag GmbH Germany, part of Springer Nature 2019

## Abstract

AlCoCrFeNi is one of the most widely studied alloy systems in the high-entropy alloy (HEA) area due to the interesting microstructure and mechanical properties. In this study, the AlCoCrFeNi alloy was prepared using spark plasma sintering (SPS) with pre-alloy powders obtained through gas atomization. Then, the sintered samples were annealed at 700, 800 and 900 °C, and the effect of annealing temperature on the microstructure, mechanical and corrosion properties was studied. The results show that phase formation takes place during annealing process with the new phase ( $\sigma$ ) and some nanoscale BCC precipitates formation. The size and quantity of the nanoscale precipitates increase with increasing annealing temperature. The twin is also observed after annealing at 900 °C. The annealing temperature has an obvious effect on the mechanical properties and corrosion resistance of the spark plasma sintered AlCoCrFeNi HEA. When the annealing temperature is 700 °C, the hardness, yield strength and fracture strength reach the maximum with the value of 545 HV, 1430 MPa and 2230 MPa, respectively. The compressive ratio reaches the maximum of 17.2%, with the annealing temperature increasing to 800 °C. The corrosion resistance of the samples decreases with increasing the annealing temperature.

**Keywords** High-entropy alloy · Phase transformation · Precipitates · Mechanical property · Corrosion resistance

## 1 Introduction

Since its introduction in 2004, high-entropy alloys (HEAs) have attracted more and more attentions, due to their promising properties including high hardness, compressive and tensile properties, excellent wear/corrosion resistance and high-temperature mechanical properties [1–10]. Unlike the traditional alloys with one or two major elements, the HEAs consist of five or more elements at equimolar or near-equimolar ratios with atomic fraction of each element being between 5 and 35 at% [3]. Most HEAs have a face-centered cubic (FCC) structure, a body-centered (BCC) structure or mixture of the two structures, and other phases ( $\sigma$  or Laves phases) are also found in some HEAs [5, 11–15].

Among the HEA systems, the AlCoCrFeNi HEA with complicated microstructure and excellent mechanical and corrosion properties have been widely studied [10, 14–18]. The AlCoCrFeNi HEA is mainly prepared by vacuum arc melting which relies on the melting of raw elemental materials by the arc (brought by the high DC current) generated between the electrode and the materials to be melt [12, 19, 20]. However, vacuum arc melting needs high energy and the phase composition is inhomogeneous which damages the mechanical properties of the alloy [11, 21, 22]. Frequently, high-temperature homogenization and further hot/cold working followed by recrystallization annealing are needed to break down the as-cast microstructure, thus obtaining homogeneous fine-grain structure materials [10, 13, 23, 24]. During recent years, alternative methods, which are largely based on traditional powder metallurgy (PM) techniques, have been proposed to fabricate AlCoCrFeNi HEA [16, 25–28]. Using PM, the AlCoCrFeNi HEA powders is obtained and consolidated into near-full-density blocky materials through sintering technology especially the spark plasma sintering (SPS) technology which has the advantages of rapid heating, short soaking time and low energy consumption [16, 25, 27, 29].

Available online at <http://link.springer.com/journal/40195>

✉ D. H. Xiao  
daihongx@csu.edu.cn

<sup>1</sup> National Key Laboratory of Science and Technology for National Defence on High-strength Structural Materials, Central South University, Changsha 410083, China

During PM, the AlCoCrFeNi HEA powders is mainly synthesized by mechanical alloying (MA) during which the pre-alloy powders are prepared by mixing raw elemental materials powders through high-energy ball milling [16, 25, 28]. However, it needs a very long time which may be up to 30 h [16] or more to acquire the HEA pre-alloy powders with solid-solution structure by high-energy ball milling. The sequence of elements addition can also affect the phase formation of the AlCoCrFeNi HEA [28]. Furthermore, the pre-alloy powders are easy to be polluted by the environment and the ball milling media, and some intermetallic or amorphous phase may generate during high-energy ball milling process [25, 28]. Ji et al. [16] prepared AlCoCrFeNi HEA by MA-SPS and obtained excellent mechanical properties with the compressive strength of 1907 MPa. The other way to prepare AlCoCrFeNi HEA powders is through gas atomization during which the raw materials are melted first and then gas-atomized to the pre-alloy powders [30–32]. Gas-atomized powders have higher purity and are more homogeneous compared to mechanical alloyed powders. Some workers have fabricated the AlCoCrFeNi HEA with excellent mechanical properties using gas-atomized powders combined with subsequent consolidation processes like laser engineered net shaping (LENS), selective electron beam melting (SEBM), etc. [31, 32]. Kuncic et al. [31] prepared the AlCoCrFeNi HEA by LENS using the gas-atomized powders, and the hardness of the alloy reaches 543 HV<sub>0.5</sub> which is higher than that of the as-cast AlCoCrFeNi HEA.

In the reported literature, heat treatment especially annealing has an obvious effect on the phases, microstructure and mechanical properties of the AlCoCrFeNi HEA [12, 13, 15]. More complicated microstructure was often reported when this alloy was annealed at moderate to high temperatures. For example, FCC phase was observed when the AlCoCrFeNi HEA was annealed at ~700 °C or higher temperature or subjected to other heat treatments [15, 20, 33, 34]. Lee and co-workers [20] prepared AlCoCrFeNi HEA through arc melting and annealing, and the results show that BCC phase transforms to FCC phase after annealing. The  $\sigma$  phase occurs when the AlCoCrFeNi HEA was annealed at 850 °C [33]. However, both the preparation of AlCoCrFeNi HEA with gas-atomized powders combined with SPS technique and the effect of annealing temperature on the spark plasma sintered AlCoCrFeNi HEA have been rarely reported.

In this work, the AlCoCrFeNi HEA was fabricated using gas-atomized pre-alloy powders combined with the SPS technique. Then, the samples were annealed for 1 h at different temperatures. The effect of annealing temperature on the phases, microstructure, mechanical and corrosion properties of the spark plasma sintered AlCoCrFeNi HEA was investigated.

## 2 Experimental

The equiatomic AlCoCrFeNi HEA pre-alloy powders were prepared using gas atomization under a high-purity Ar atmosphere with the high purity of 99.99 wt% of Al, Co, Cr, Fe and Ni as raw materials. The atomization pressure was 4 MPa. Then, the AlCoCrFeNi HEA pre-alloy powders (–400 mesh) were sintered by SPS (FCT, HP D25/3) at 1200 °C for 10 min with a diameter of 40 mm in Ar atmosphere under the pressure of 30 MPa and heating rate of 50 °C/min. After SPS, the samples were annealed at 700 °C, 800 °C and 900 °C for 1 h, respectively. For the convenience of the following study, the spark plasma sintered and annealed samples under different temperatures of 700 °C, 800 °C and 900 °C were numbered as Sample 1, Sample 2, Sample 3 and Sample 4, respectively.

The phases of the sintered and annealed samples were characterized under X-ray diffractometer (XRD, SIEMENS D500) with Cu  $K\alpha$  radiation, through  $2\theta$  ranging from 20° to 90° with a scan rate of 4 °/min. Scanning electron microscope (SEM, Nova Nano 230, FEI) equipped with an energy-dispersive spectroscopy (EDS) system was used to study the microstructure of the samples. The bright-field images and selected area diffraction patterns (SADP) were obtained using transmission electron microscopy (TEM, Tecnai G2 F20, FEI). The distribution of elements in the samples was tested by electron probe micro-analysis (EPMA, JXA-8530F, Japan). The hardness of the sintered and annealed samples was tested on the Vickers hardness tester (Micromet 5104) at a load of 100 g. Five random indents were performed for each sample. Compression tests were performed on the samples with a dimension of  $\varphi$  4 mm  $\times$  8 mm using the Instron 3369 testing machine at a strain rate of  $1 \times 10^{-4} \text{ s}^{-1}$  under room temperature. The tests were repeated three times. The electrochemical experiments were conducted using the CHI660C electrochemical test equipment at room temperature. The test solution was 0.5 mol/L H<sub>2</sub>SO<sub>4</sub> solution, and the scan rate was 5 mV/s.

## 3 Results and Discussion

### 3.1 XRD Diffraction Analysis

The XRD patterns of the AlCoCrFeNi HEA are presented in Fig. 1. In Fig. 1a, three phases are found in the spark plasma sintered AlCoCrFeNi HEA, including B2, BCC and FCC phases, which are different from the as-cast AlCoCrFeNi HEA normally exhibiting BCC phase-dominated microstructure with the coexistence of

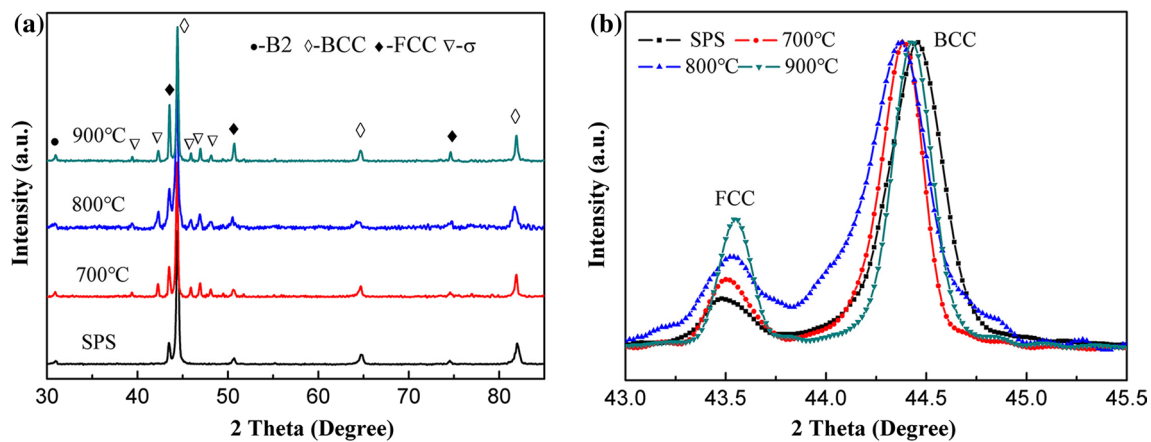


**Fig. 1** XRD patterns of the spark plasma sintered and annealed samples **a**, and the enlarged region of two theta ranging between 43° and 45.5° **b**

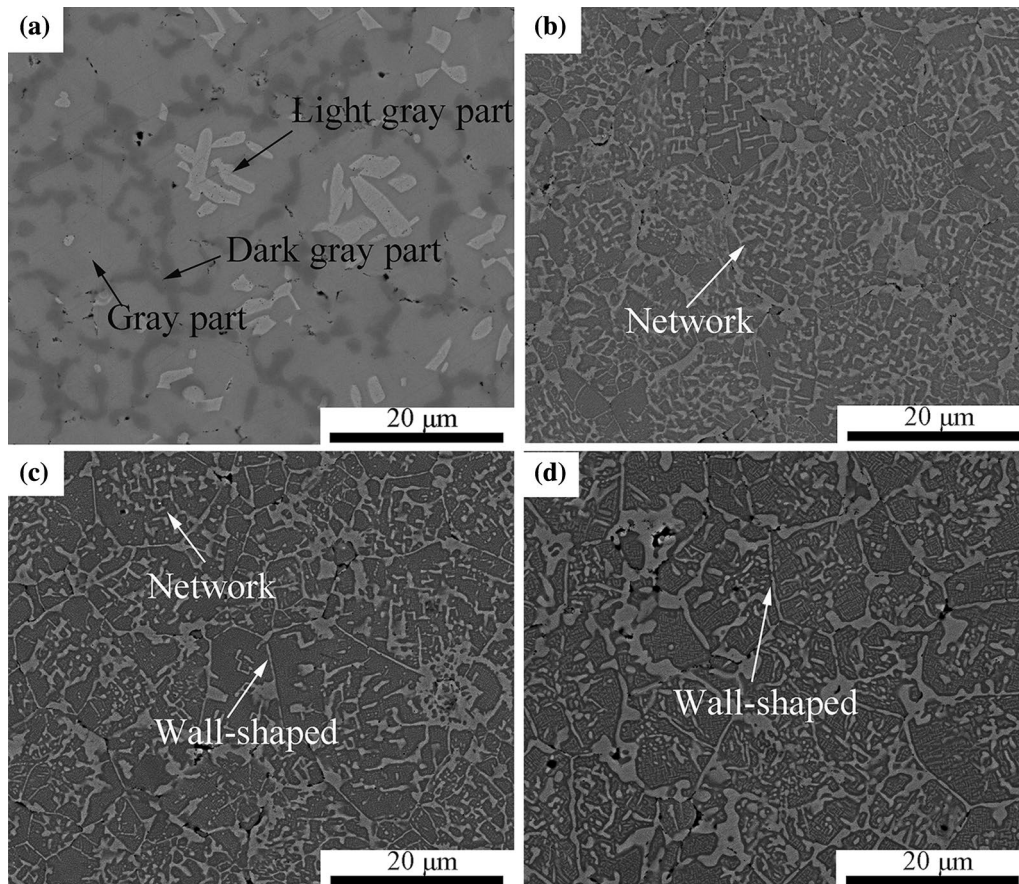
B2 phase [13]. The FCC phase is also observed in the sample prepared by MA-SPS which is consistent with this work, and it is thought that the FCC phase formation may be associated with the critical conditions of the non-equilibrium process of rapid sintering during SPS, and the large pulsed electric current of SPS might also lead to uncertain phase evolution [16]. Except for the three main phases, a new phase ( $\sigma$  phase) is also detected after annealing, indicating that phase transformation takes place during annealing process. No additional phase can be detected with increasing the annealing temperature from 700 to 900 °C. These results are consistent with Butler's CALPHAD results [34].

In order to investigate the impacts of annealing temperature on the phases of the spark plasma sintered AlCoCrFeNi HEA, the main peaks of FCC and BCC/B2 phases in the XRD are enlarged and the results are shown in Fig. 1b. Based on the relative peak intensity of the XRD patterns, the FCC phase increases with increasing the annealing temperature, showing that annealing can promote FCC phase generation and the FCC phase content is positively correlated with the annealing temperature. Moreover, the FCC peaks shift toward high-angle side as the annealing temperature increases, indicating that annealing can reduce lattice distortion. However, the BCC/B2 peaks move to low-angle side after annealing, which indicates that the lattice distortion of the BCC/B2 phase increases after annealing. Munitz et al. [12] thought that the shift of the FCC phase in the AlCoCrFeNi HEA during annealing is due to Al concentration in the phases. In this work, the Al content changes both in FCC and BCC/B2 phases, due to part of BCC/B2 phase transforms to FCC and  $\sigma$  phases during annealing process, which results in the peak shift of the FCC and BCC/B2 phases.

### 3.2 Microstructures

Figure 2 shows the microstructure of the spark plasma sintered and annealed samples. In Fig. 2a, no obvious particles are observed and only some small pores are detected, indicating that the spark plasma sintered sample has been fully sintered at 1200 °C for 10 min. Three contrast areas can be detected, including dark gray part, gray part and light gray part. The EDS results of the three areas are shown in Table 1. Based on the relative peak intensity in the XRD patterns and the EDS results, the dark gray part with Cr being up to 85.84% is Cr-rich BCC phase, the gray part is Al-, Ni-rich B2 phase and the light gray part is Fe-, Cr- and Co-rich FCC phase.

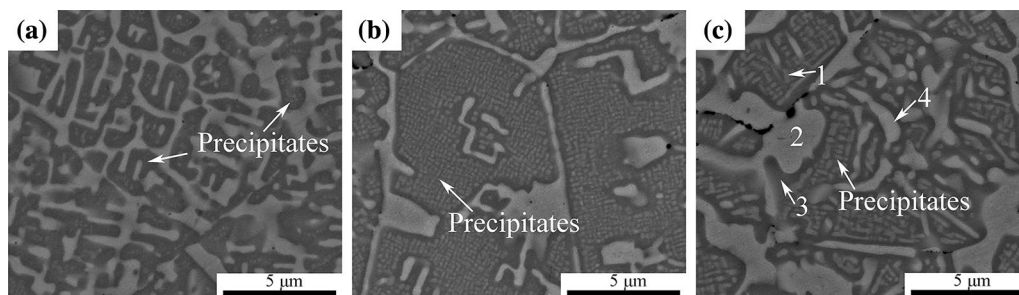
After annealing, the dark gray part disappears and the network structure occurs as shown in Fig. 2b–d. Moreover, the network structure reduces and the wall-shaped structure increases with increasing the annealing temperature. The wall-shaped structure becomes coarse at the higher annealing temperature (above 800 °C). The high-magnification microstructure of the annealed samples is presented in Fig. 3. The nanoscale precipitates (labeled 1) are observed in the matrix phase after annealing. With furtherly increasing the annealing temperature, both the size and quantity of the nanoscale precipitates increase, indicating that annealing can promote the nanoscale precipitates generate. Except for the nanoscale precipitates, three contrast phases are also observed, namely the light gray, gray and white gray phases which are marked as 2, 3 and 4 in Fig. 3, respectively. The EDS results as shown in Table 2 indicate that the nanoscale precipitates are the BCC phases with the five elements of near-equimolar ratio, the gray phase is Al-, Ni-rich B2 phase, the light gray phase is Fe-, Cr-, Co-rich FCC phase, and the white gray phase is Cr-, Fe-rich  $\sigma$  phase. These observations



**Fig. 2** Microstructures of **a** Sample 1, **b** Sample 2, **c** Sample 3, **d** Sample 4

**Table 1** Chemical compositions (at%) of phases in the spark plasma sintered sample

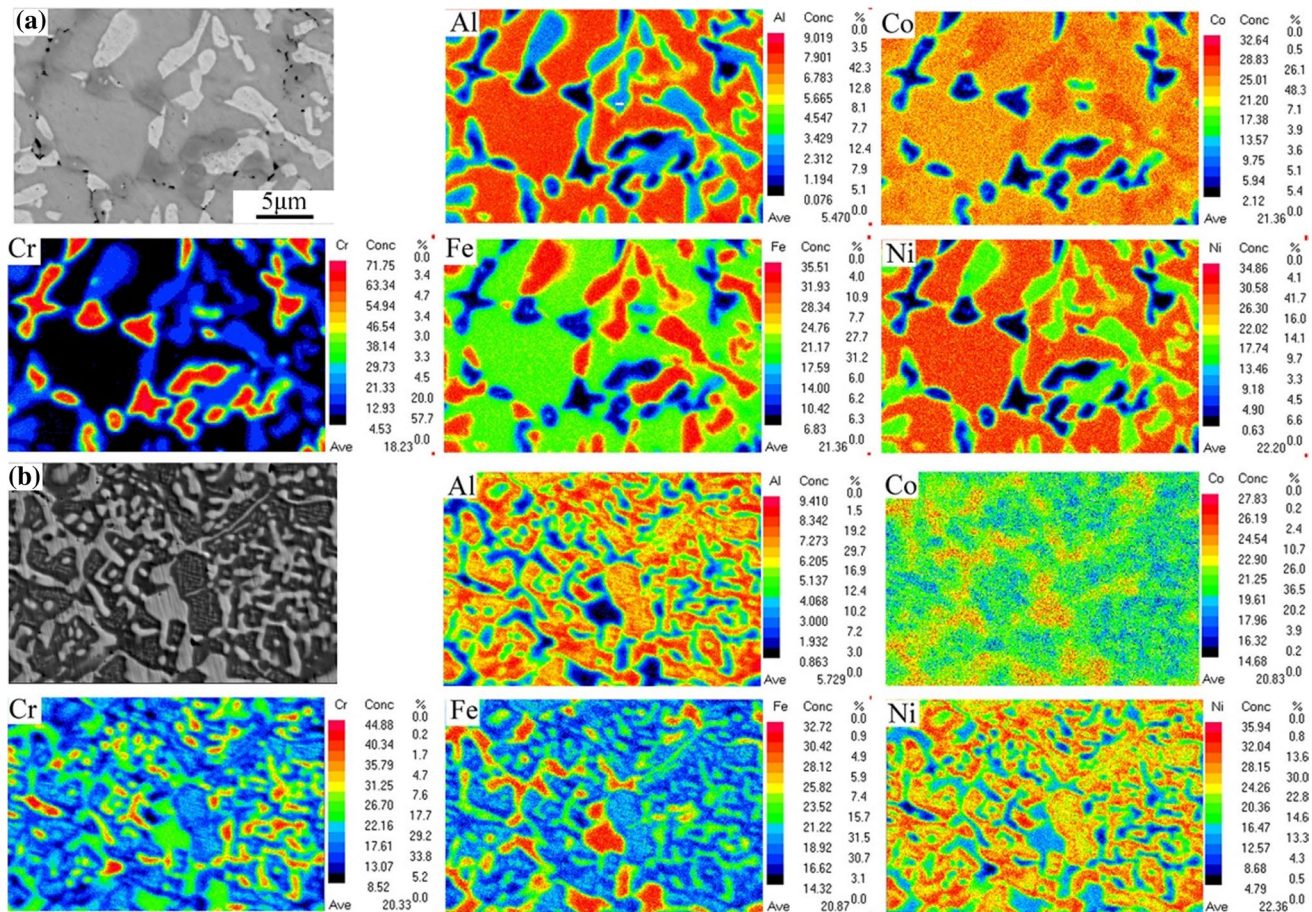
| Regions    | Phase | Al    | Cr    | Fe    | Co    | Ni    |
|------------|-------|-------|-------|-------|-------|-------|
| Light gray | FCC   | 8.7   | 14.59 | 33.28 | 26.67 | 16.76 |
| Dark gray  | BCC   | 0.58  | 85.84 | 8.93  | 3.47  | 1.18  |
| Gray       | B2    | 26.58 | 6.45  | 19.04 | 22.19 | 25.74 |



**Fig. 3** High-magnification microstructures of **a** Sample 2, **b** Sample 3, **c** Sample 4 annealed at different temperatures

**Table 2** Chemical compositions (at%) of phases in the annealed samples

| Regions          | Phase    | Al    | Cr    | Fe    | Co    | Ni    |
|------------------|----------|-------|-------|-------|-------|-------|
| Precipitates (1) | BCC      | 22.97 | 17.57 | 18.29 | 19.16 | 22.01 |
| Light gray (2)   | FCC      | 4.92  | 25.89 | 31.77 | 24.10 | 13.42 |
| Gray (3)         | B2       | 27.58 | 11.42 | 15.71 | 19.53 | 25.76 |
| White gray (4)   | $\sigma$ | 5.87  | 43.56 | 25.06 | 18.88 | 6.61  |

**Fig. 4** EPMA mapping images of **a** Sample 1 and **b** Sample 4

are similar to Butler's study [34]. Rao et al. [35] thought that the existence of Cr element and binary systems of the Cr–Co, Cr–Fe, and Cr–Ni can help to form the  $\sigma$  phase in the Al<sub>x</sub>CoCrFeNi HEA. Compared to the XRD patterns, the BCC and B2 phases' peaks are not distinguished, indicating that BCC and B2 phases have similar lattice parameters [36].

EPMA mapping (Fig. 4a, b) was done for Sample 1 and Sample 4 to visualize elemental distribution in the spark plasma sintered and annealed samples. In Fig. 4a, it can be seen that FCC phase is significantly depleted with Al and there is a Cr-rich BCC area. B2 matrix phase is rich of Al and Ni elements, and Co element distributes uniformly both in B2 matrix and FCC phase. The EPMA mapping results of the spark plasma sintered sample are consistent with the

results of SEM and EDS. After annealed at 900 °C for 1 h, Al and Ni elements mainly distribute in B2 matrix and precipitate phases, Fe and Co elements mainly distribute in the light gray (FCC) phase, and Cr element mainly distributes in the white gray ( $\sigma$ ) phase, which is consistent with Fig. 3c and Table 2. According to the results of EDS, SEM and EMPA, it can be seen that the quantity of Fe, Co, Ni both in FCC and B2 matrix phases changes little. The amount of Al element in FCC, BCC and B2 matrix phases has an obvious change, which may result in the peak shift of FCC and BCC/B2 phases [12]. The amount of Cr in FCC and B2 matrix phases increases from ~14 (Sample 1) to ~26 at% (Sample 4) and from ~6 (Sample 1) to ~11 at% (Sample 4), respectively. After annealing, the bulk Cr-rich BCC phase

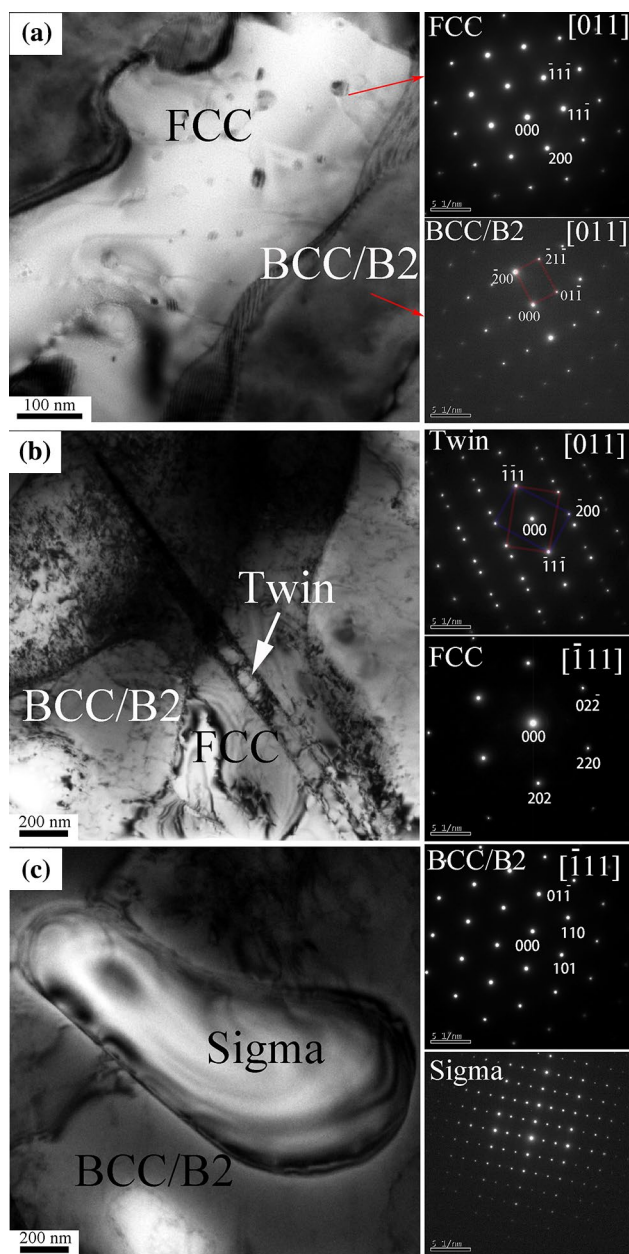


**Fig. 5** TEM bright-field images and the corresponding selected area electron diffraction patterns of **a** Sample 1, **b** and **c** Sample 4

disappears, and a new phase ( $\sigma$  phase) consisted of  $\sim 45\%$  Cr forms. It can be inferred that most of the Cr element in Cr-rich BCC phase diffuses into nanoscale precipitates, FCC and B2 matrix phases, and the remaining Cr element forms Cr-, Fe-rich  $\sigma$  phase during annealing.

In order to further study the impact of annealing on the microstructure, TEM analysis of Sample 1 and Sample 4 was done. For Sample 1, FCC and BCC/B2 phases are detected, as shown in Fig. 5a. After annealing at  $900\text{ }^\circ\text{C}$  for 1 h, except for the BCC/B2 and FCC phases, the  $\sigma$  phase with tetragonal structure in the BCC/B2 phase is also observed, as labeled

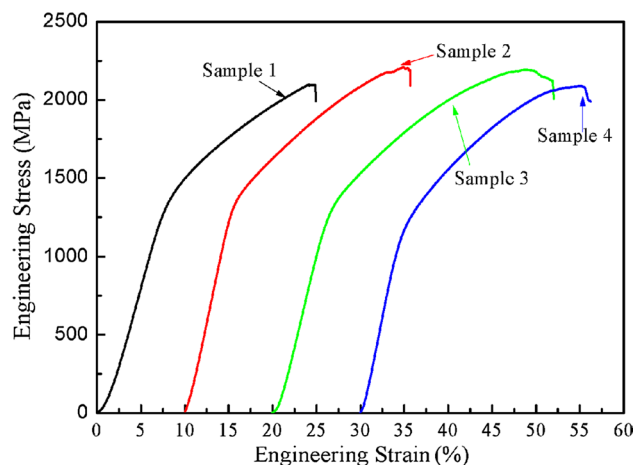


**Fig. 6** Room-temperature compressive stress–strain curves of the samples

in Fig. 5c, indicating that the  $\sigma$  phase is mainly transformed from BCC/B2 phase. What is more, the twin with FCC structure is found after annealing at  $900\text{ }^\circ\text{C}$  for 1 h, as presented in Fig. 5b. The annealing twin has not been observed from previous studies on the same alloy systems.

### 3.3 The Mechanical Properties of the Samples

The room-temperature compressive stress–strain curves of the samples are shown in Fig. 6, and the compression properties and hardness of the samples are summarized in Table 3. The hardness, yield strength ( $\sigma_{0.2}$ ), fracture strength ( $\sigma_f$ ) and compressive ratio ( $\epsilon_f$ ) of Sample 1 are  $\sim 497\text{ HV}$ ,  $\sim 1390\text{ MPa}$ ,  $\sim 2150\text{ MPa}$  and  $\sim 12\%$ , respectively. After annealed at  $700\text{ }^\circ\text{C}$  for 1 h, the hardness, yield strength ( $\sigma_{0.2}$ ), fracture strength ( $\sigma_f$ ) and compressive ratio ( $\epsilon_f$ ) increase to  $\sim 545\text{ HV}$ ,  $\sim 1430\text{ MPa}$ ,  $\sim 2230\text{ MPa}$  and  $\sim 13\%$ , respectively. With increasing the annealing temperature to  $800\text{ }^\circ\text{C}$ , the yield strength ( $\sigma_{0.2}$ ) and fracture strength ( $\sigma_f$ ) decrease to  $\sim 1350\text{ MPa}$  and  $\sim 2195\text{ MPa}$ , respectively. The hardness has no obvious change, while the fracture compressive ratio increases to  $\sim 17\%$ . However, with further increasing the annealing temperature from  $800$  to  $900\text{ }^\circ\text{C}$ , all of the mechanical properties decrease, with the hardness, yield strength ( $\sigma_{0.2}$ ), fracture strength ( $\sigma_f$ ) and compressive

**Table 3** Mechanical properties of the samples

| Sample   | Hardness (HV) | $\sigma_{0.2}$ (MPa) | $\sigma_f$ (MPa) | $\epsilon_f$ (%) |
|----------|---------------|----------------------|------------------|------------------|
| Sample 1 | $497 \pm 13$  | $1390 \pm 15$        | $2150 \pm 17$    | $12.1 \pm 0.3$   |
| Sample 2 | $545 \pm 8$   | $1430 \pm 18$        | $2230 \pm 14$    | $13.3 \pm 0.2$   |
| Sample 3 | $544 \pm 9$   | $1350 \pm 16$        | $2195 \pm 18$    | $17.2 \pm 0.3$   |
| Sample 4 | $458 \pm 12$  | $1120 \pm 14$        | $2090 \pm 15$    | $15.0 \pm 0.4$   |

ratio ( $\epsilon_f$ )  $\sim$  458 HV,  $\sim$  1120 MPa,  $\sim$  2090 MPa and  $\sim$  15%, respectively.

The strengthening mechanisms in polycrystalline materials are traditionally summarized into four categories: solid-solution strengthening, precipitation strengthening, grain-boundary strengthening and dislocation strengthening [37]. Except for the four basic strengthening mechanisms, the phase transformation also plays an important role in the mechanical properties of the HEA. For this work, the phase transformation strengthening and precipitation strengthening are the main mechanisms. According to the results in Figs. 1, 2, 3 and 4, phase transformation takes place during annealing process with Cr-rich BCC phase disappearing and  $\sigma$  phase appearing. What is more, the content of BCC and FCC phases alters and the structure of FCC phase changes. The BCC phase is helpful to the hardness and strength, and the FCC phase is good for the high ductility and low strength of the alloy [24]. Except for the content of BCC phase,  $\sigma$  phase which is hard and brittle can also contribute to the hardness and strength of the samples [12]. Besides the phase transformation strengthening, the precipitates strengthening is also an important strengthening mechanism in this study. In Figs. 2, 3, 4 and 5, it can be known that nanoscale BCC

and  $\sigma$  precipitates are formed after annealing, which could improve the hardness and strength of the annealed samples [38]. The nanoscale precipitates are expected to produce strengthening effect, either through a dislocation bypass mechanism (Orowan-type) or through particle shearing mechanism [39, 40]. Orowan mechanism dominates when particles exceed a critical size or are incoherent with the matrix. However, the shearing mechanism dominates when particles are sufficiently small and coherent with the matrix [40, 41]. The nanoscale BCC and  $\sigma$  precipitates in the matrix (Figs. 3 and 5) maybe cause particle shearing mechanism in the annealed samples. Generally, the mechanical properties are positively correlated with the number and inversely related to the size of the precipitates [42]. However, the quantity and the size of the precipitates increase obviously with increasing the annealing temperature (Fig. 3), which reduces the precipitation strengthening effect, so that the yield strength ( $\sigma_{0.2}$ ) and fracture strength ( $\sigma_f$ ) decrease with increasing the annealing temperature above 800 °C. Moreover, the solid-solution, grain-boundary, dislocation and other factors, such as the annealing twin (Fig. 4b), can also affect the mechanical properties of the annealed samples [40].

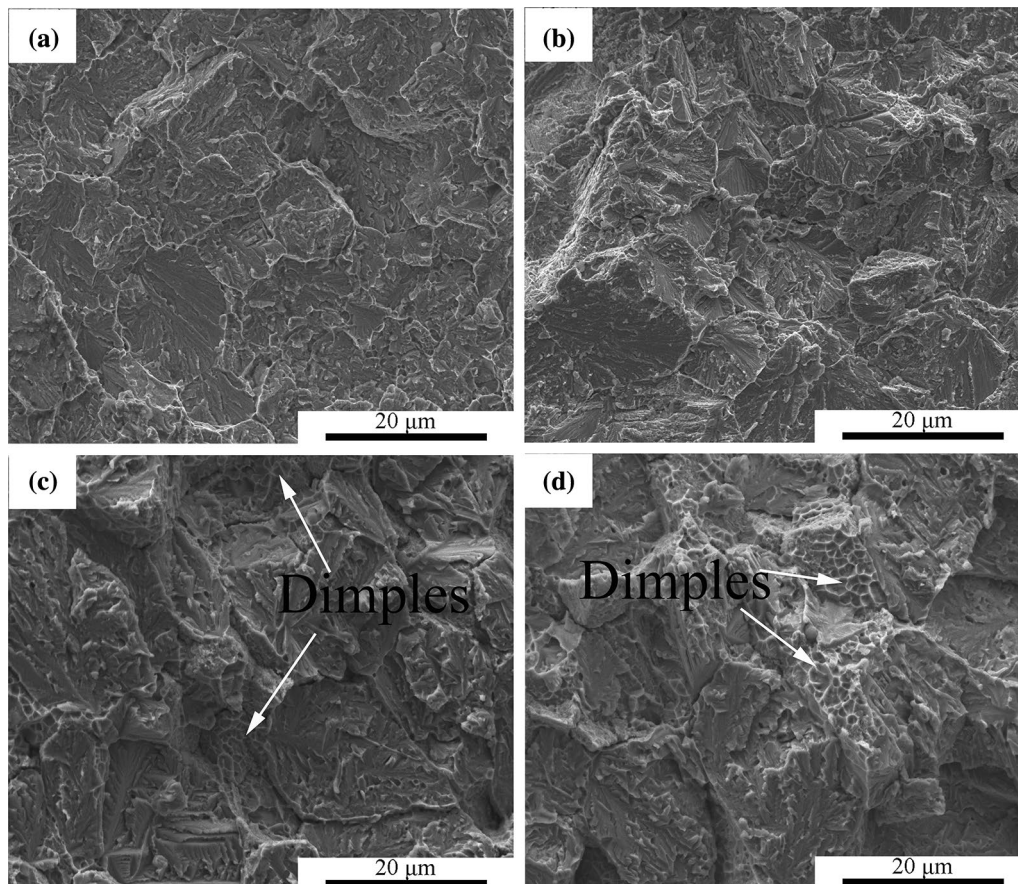


**Fig. 7** Compressed fractographic feature of **a** Sample 1, **b** Sample 2, **c** Sample 3, **d** Sample 4

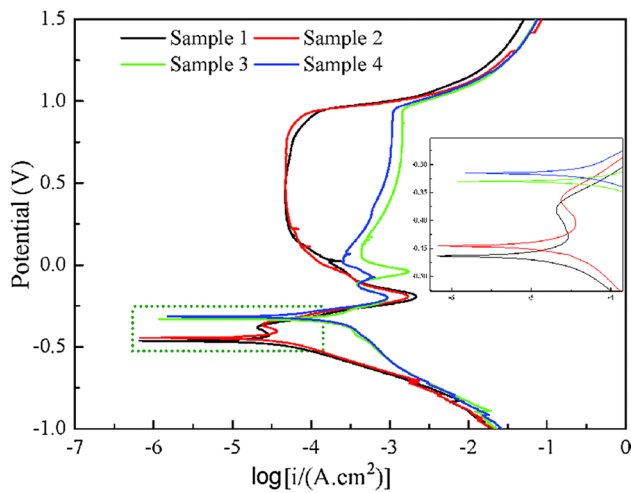


**Fig. 8** Polarization curves of the samples

**Table 4** Dynamic parameters derived from the potentiodynamic polarization curves by linear fitting

| Sample   | $E_{\text{corr}}$ (V vs. SCE) | $I_{\text{corr}}$ ( $\mu\text{A}/\text{cm}^2$ ) | $R_p$ ( $\Omega$ ) |
|----------|-------------------------------|---|--------------------|
| Sample 1 | -0.463                        | 17.8  | 1388.8             |
| Sample 2 | -0.445                        | 19.2  | 1246.8             |
| Sample 3 | -0.363                        | 89.1  | 629.3              |
| Sample 4 | -0.315                        | 108.0   | 401.2              |

Figure 7 exhibits the corresponding fractographic feature of the samples. Cleavage steps can be observed in the four samples. Some tear ridges are also observed in Sample 1 and Sample 2 (Fig. 7a, b). With increasing annealing temperature, some dimples are also detected in Sample 3 and Sample 4 (Fig. 7c, d), which contribute to the plasticity of the samples. It can be concluded that the fracture mechanism of the samples is cleavage fracture.

### 3.4 Corrosion Behavior of the Samples

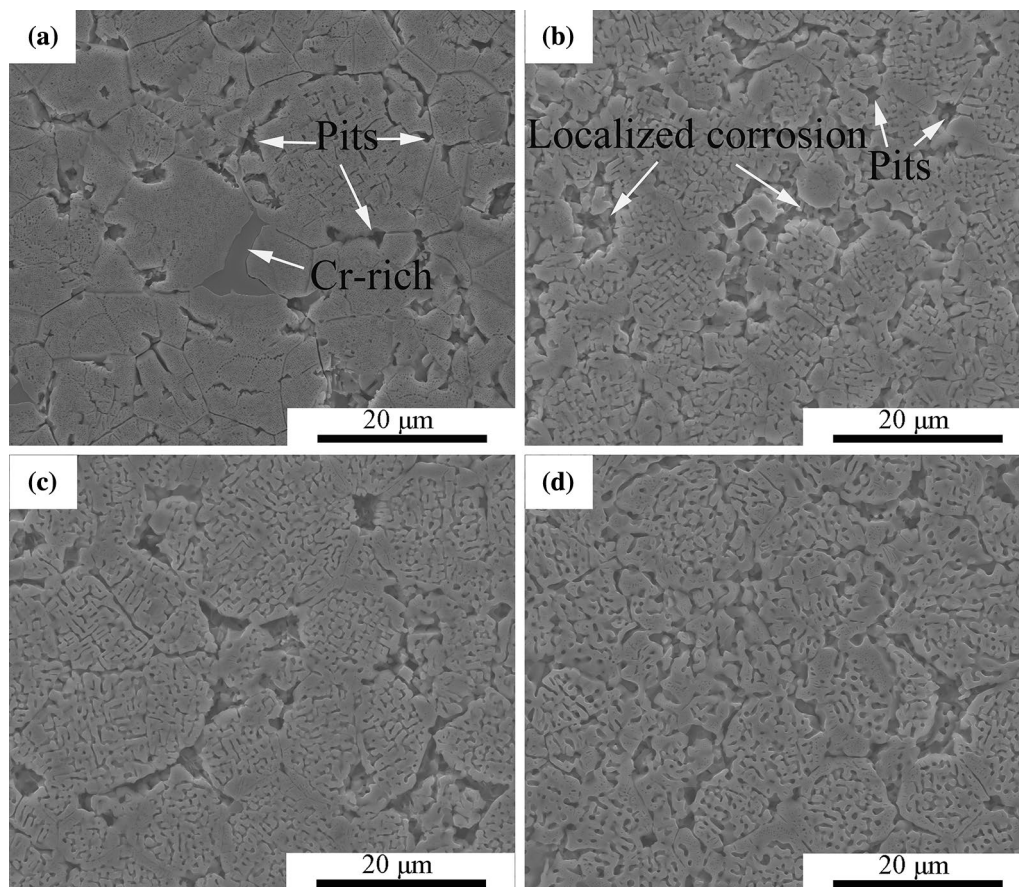
The electrochemical corrosion behavior of the samples was studied at room temperature, and the polarization curves are shown in Fig. 8. From Fig. 8, it can be seen that all of the four samples have passivation region, probably because the Cr-rich BCC phases are oxidized to passive oxide film. What is more, the existence of Al also helps to form the passive oxide film [14]. Zhang et al. [43] thought that the addition of Al might enlarge the passive region by bringing in  $\alpha\text{-AlO}(\text{OH})/\alpha\text{-Al}_2\text{O}_3$  during the whole corrosion process. Except for the passivation region, all of the samples have the secondary passivation region, which is mainly attributed to the further oxidation or hydroxidation of the passive oxide film, thus altering the valence of Cr [44].

Table 4 reveals the corrosion potential ( $E_{\text{corr}}$ ), corrosion current density ( $I_{\text{corr}}$ ) and polarization resistance ( $R_p$ ) of the four samples. It can be seen that the  $E_{\text{corr}}$ ,  $I_{\text{corr}}$  and  $R_p$  of Sample 1 are  $-0.463$  V,  $17.8 \mu\text{A}/\text{cm}^2$  and  $1388.8 \Omega$ , respectively. The  $E_{\text{corr}}$  and  $I_{\text{corr}}$  increase and the  $R_p$  decreases with increasing annealing temperature. Sample 4 has the highest  $E_{\text{corr}}$  and  $I_{\text{corr}}$ , and the lowest  $R_p$  of  $-0.315$  V,  $108 \mu\text{A}/\text{cm}^2$  and  $401.2 \Omega$ , respectively. In general, the corrosion rate is positively correlated with  $I_{\text{corr}}$  [45], so that the results of electrochemical corrosion behavior indicate that the corrosion resistance of the samples decreases with increasing annealing temperature. In the dissolution morphologies of the four samples after the polarization tests as shown in Fig. 9, the pitting corrosion intensifies and some localized corrosion can be observed with increasing annealing temperature. In Fig. 9, FCC phase is mainly corroded, showing that FCC phase is more susceptible to corrosion than BCC/B2 phase. As reported [5], the Cr-rich phase could form the  $\text{Cr}_2\text{O}_3$  passive oxide film which could prevent the matrix from being further corroded. According to the thermodynamic study, the breaking down of  $\text{CoCr}_2\text{O}_4$  and  $\text{CoFe}_2\text{O}_4$  could also dominate the pitting behavior and impair the corrosion resistance [43]. Shang et al. [46] also reported that galvanic corrosion that occurred around  $\sigma$  phase dominated the corrosion process and  $\sigma$  phase could decrease the corrosion resistance of the sample. In this work, Cr-rich BCC phase disappears and  $\sigma$  phase forms during annealing process, which results in a reduction in corrosion resistance after annealing. Meanwhile, BCC/B2 phase shows a better corrosion resistance than FCC phase. In the microstructure, FCC phase increases and the Cr-rich BCC phase transforms to other phases, resulting in the decrease in the corrosion resistance with increasing the annealing temperature.

## 4 Conclusion

In this study, AlCoCrFeNi HEA has been prepared using gas atomization combined with SPS technique. The effect of annealing temperature on the microstructure, mechanical and corrosion properties of the spark plasma sintered AlCoCrFeNi HEA has been studied, and the results are as follows: (1) There is phase transformation during annealing process with the B2 + BCC + FCC phases in the spark plasma sintered sample transforming to B2 + BCC + FCC +  $\sigma$  phases in the annealed samples; (2) except for the  $\sigma$  phase and nanoscale precipitates, the annealed twin is also observed after annealing at  $900^\circ\text{C}$ ; (3) annealing temperature has an obvious effect on the mechanical properties of the samples, with the highest hardness, yield strength, fracture strength and compressive ratio 545 HV, 1420 MPa, 2236 MPa and 17.2%, respectively; (4) the corrosion resistance of the spark





**Fig. 9** Dissolution morphologies of the four samples after the polarization tests: **a** Sample 1, **b** Sample 2, **c** Sample 3, **d** Sample 4

plasma sintered AlCoCrFeNi HEA decreases with increasing annealing temperature.

**Acknowledgements** The authors gratefully acknowledge the financial support from the Natural Science Foundation of Hunan (China) (No. 2016JJ214) and the Natural Science Foundation of China (No. 51874369).

## References

- [1] O.N. Senkov, C. Woodward, S.V. Senkova, D.B. Miracle, *J. Mater. Sci.* **47**, 6522 (2012)
- [2] Y.X. Zhuang, W.J. Liu, P.F. Xing, F. Wang, J.C. He, *Acta Metall. Sin. (Engl. Lett.)* **25**, 124 (2012)
- [3] Y. Zhang, T.T. Zuo, Z. Tang, M.C. Gao, K.A. Dahmen, P.K. Liaw, Z.P. Lu, *Prog. Mater. Sci.* **6**, 11 (2014)
- [4] Y. Zou, J.M. Wheeler, H. Ma, P. Okle, R. Spolenak, *Nano Lett.* **17**, 1569 (2017)
- [5] D.H. Xiao, P.F. Zhou, W.Q. Wu, H.Y. Diao, M.C. Gao, M. Song, P.K. Liaw, *Mater. Design* **116**, 438 (2017)
- [6] P.F. Zhou, D.H. Xiao, Z. Wu, X.Q. Ou, *Mater. Sci. Eng. A* **739**, 86 (2019)
- [7] J.W. Yeh, S.K. Chen, S.J. Lin, J.Y. Gan, T.S. Chin, T.T. Shun, C.H. Tsau, S.Y. Chang, *Adv. Eng. Mater.* **6**, 299 (2004)
- [8] A. Kumar, A.K. Swarnakar, M. Chopkar, *J. Mater. Eng. Perform.* **27**, 3304 (2018)
- [9] B. Gludovatz, A. Hohenwarter, D. Catoor, E.H. Chang, E.P. George, Q.O. Ritchie, *Science* **345**, 1153 (2014)
- [10] Y.Z. Shi, L. Collins, R. Feng, C. Zhang, N. Balke, P.K. Liaw, B. Yang, *Corros. Sci.* **133**, 120 (2018)
- [11] J. Chen, P.Y. Niu, Y.Z. Liu, Y.K. Lu, X.H. Wang, Y.L. Peng, J.N. Liu, *Mater. Design* **94**, 39 (2016)
- [12] A. Munitz, S. Salhov, S. Hayun, N. Frage, *J. Alloys Compd.* **683**, 221 (2016)
- [13] Z. Tang, O.N. Senkov, C.M. Parish, C. Zhang, F. Zhang, L.J. Santodonato, G.Y. Wang, G.F. Zhao, F.Q. Yang, P.K. Liaw, *Mater. Sci. Eng. A* **647**, 229 (2015)
- [14] Y.Z. Shi, B. Yang, X. Xie, J. Brechtel, K.A. Dahmen, P.K. Liaw, *Corros. Sci.* **119**, 33 (2017)
- [15] W.R. Wang, W.L. Wang, J.W. Yeh, *J. Alloys Compd.* **589**, 143 (2014)
- [16] W. Ji, Z.Y. Fu, W.M. Wang, H. Wang, J.Y. Zhang, Y.C. Wang, F. Zhang, *J. Alloys Compd.* **589**, 61 (2014)
- [17] Z.M. Jiao, Z.H. Wang, R.F. Wu, J.W. Qiao, *Appl. Phys. A* **122**, 794 (2016)
- [18] J. Joseph, N. Stanford, P. Hodgson, D.M. Fabijanic, *J. Alloys Compd.* **726**, 885 (2017)
- [19] Y.K. Lv, R.Y. Hu, Z.H. Yao, J. Chen, D.P. Xu, Y. Liu, X.H. Fan, *Mater. Design* **132**, 392 (2017)
- [20] K.S. Lee, J.H. Kang, K.R. Lim, Y.S. Na, *Mater. Charact.* **132**, 162 (2017)
- [21] G. Muthupandi, K.R. Lim, Y.S. Na, J. Park, D. Lim, H. Kim, S. Park, Y.S. Choi, *Mater. Sci. Eng. A* **696**, 146 (2017)

- [22] N.G. Jones, R. Izzo, P.M. Mignanelli, K.A. Christofidou, H.J. Stone, *Intermetallics* **71**, 43 (2016)
- [23] E. Ghassemali, R. Sonkusare, K. Biswas, N.P. Gurao, *J. Alloys Compd.* **710**, 539 (2017)
- [24] Y.F. Kao, T.J. Chen, S.K. Chen, J.W. Yeh, *J. Alloys Compd.* **488**, 57 (2009)
- [25] S. Mohanty, T.N. Maity, S. Mukhopadhyay, S. Sarkar, N.P. Gurao, S. Bhowmick, K. Biswas, *Mater. Sci. Eng. A* **679**, 299 (2017)
- [26] A.J. Zhang, J.S. Han, J.H. Meng, B. Su, P.D. Li, *Mater. Lett.* **181**, 82 (2016)
- [27] E. Colombini, R. Rosa, L. Trombi, M. Zadra, A. Casagrande, P. Veronesi, *Mater. Chem. Phys.* **210**, 78 (2018)
- [28] M. Vaidya, A. Prasad, A. Parakh, B.S. Murty, *Mater. Design* **126**, 37 (2017)
- [29] D. Giuntini, E.A. Olefsky, C.G. Cardona, A.L. Maximenko, M.S. Yurlova, C.D. Haines, D.G. Martin, D. Kapoor, *Materials* **6**, 2612 (2013)
- [30] P.P. Ding, A.Q. Mao, X. Zhang, X. Jin, B. Wang, M. Liu, X.L. Gu, *J. Alloys Compd.* **721**, 609 (2017)
- [31] I. Kuncce, M. Polanski, K. Karczewski, T. Plocinski, K.J. Kurzydowski, *J. Alloys Compd.* **648**, 751 (2015)
- [32] H. Shiratori, T. Fujieda, K. Yamanaka, Y. Koizumi, K. Kuwabara, T. Kato, A. Chiba, *Mater. Sci. Eng. A* **656**, 39 (2016)
- [33] R. Wang, K. Zhang, C. Davies, X.H. Wu, *J. Alloys Compd.* **694**, 971 (2017)
- [34] T.M. Butler, M.L. Weaver, *J. Alloys Compd.* **691**, 119–129 (2017)
- [35] J.C. Rao, H.Y. Diao, V. Ocelík, D. Vainchtein, C. Zhang, C. Kuo, Z. Tang, W. Guo, J.D. Poplawsky, Y. Zhou, P.K. Liaw, J.T.M.D. Hosson, *Acta Mater.* **131**, 206 (2017)
- [36] L.J. Santodonato, Y. Zhang, M. Feyngenson, C.M. Parish, M.C. Gao, R.J.K. Weber, J.C. Neuefeind, Z. Tang, P.K. Liaw, *Nat. Commun.* **6**, 5964 (2015)
- [37] J.Y. He, H. Wang, H.L. Huang, X.D. Xu, M.W. Chen, Y. Wu, X.J. Liu, T.G. Nieh, K. An, Z.P. Lu, *Acta Mater.* **102**, 187 (2016)
- [38] Y.F. Wang, S.G. Ma, X.H. Chen, J.Y. Shi, Y. Zhang, J.W. Qiao, *Acta Metall. Sin. (Engl. Lett.)* **26**, 277 (2013)
- [39] N.Q. Vo, C.H. Liebscher, M.J.S. Rawlings, M. Asta, D.C. Dunand, *Acta Mater.* **71**, 89 (2014)
- [40] W.Q. Wu, R. Zhou, B.Q. Wei, S. Ni, Y. Liu, M. Song, *Mater. Charact.* **144**, 605 (2018)
- [41] L. Zhang, Y. Zhou, X. Jin, X.Y. Du, B.S. Li, *Mater. Sci. Eng. A* **732**, 186 (2018)
- [42] Y.T. Wang, J.B. Li, Y.C. Xin, X.H. Chen, M. Rashad, B. Liu, Y. Liu, *Acta Metall. Sin. (Engl. Lett.)* **32**, 932 (2019)
- [43] B.L. Zhang, Y. Zhang, S.M. Guo, *J. Mater. Sci.* **53**, 14729 (2018)
- [44] Y.F. Kao, T.D. Lee, S.K. Chen, Y.S. Chang, *Corros. Sci.* **52**, 1026 (2010)
- [45] J.B. Cheng, D. Liu, X.B. Liang, B.S. Liu, *Acta Metall. Sin. (Engl. Lett.)* **27**, 1031 (2014)
- [46] X.L. Shang, Z.J. Wang, Q.F. Wu, J.C. Wang, J.J. Li, J.K. Yu, *Acta Metall. Sin. (Engl. Lett.)* **32**, 41 (2019)